Supplementary Information for

The critical role of electrochemically-activated adsorbates in neutral OER

Longsheng Zhang[1], Haiyang Yuan[2], Liping Wang[1], Hui Zhang[3], Yijing Zang[3], Yao Tian[4], Yunzhou Wen[1], Fenglou, Ni[1], Hao Song[4], Haifeng Wang[2*], Bo Zhang[1*] & Huisheng Peng[1*]

[1]*State Key Laboratory of Molecular Engineering of Polymers, Department of Macromolecular Science and Laboratory of Advanced Materials, Fudan University, Shanghai, 200438, China*

[2]*Key Laboratory for Advanced Materials, Key Laboratory for Advanced Materials, Centre for Computational Chemistry and Research Institute of Industrial Catalysis, East China University of Science and Technology, Shanghai 200237, China*

[3]*State Key Laboratory of Functional Materials for Informatics, Shanghai Institute of Microsystem and Information Technology, Chinese Academy of Sciences, CAS Center for Excellence in Superconducting Electronics, Shanghai 200050, China*

[4]*Key Laboratory of Systems Bioengineering, School of Chemical Engineering and Technology, SynBio Research Platform, Collaborative Innovation Centre of Chemical Science and Engineering, Tianjin University, Tianjin 300072, China*

*Correspondence and requests for materials should be addressed to Huisheng Peng (penghs@fudan.edu.cn) (Peng HS), Bo Zhang (bozhang@fudan.edu.cn) (Zhang B), Haifeng Wang (hfwang@ecust.edu.cn) (Wang HF).

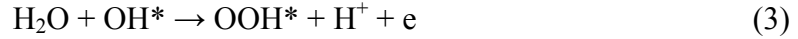**This file includes:**

Materials and Methods

Supplementary Figures

Supplementary Tables

References

1 Materials and Methods

1.1 Computational details

Density functional theory (DFT) calculations were carried out with the Perdew-Burke-Ernzerhof (PBE) functional within the generalized gradient approximation (GGA) [1]. All calculations were performed using the Vienna Ab-initio Simulation Package (VASP) [2]. The electron-ion interaction was treated with the project-augmented wave (PAW) method [3]. The plane wave basis sets with an energy cutoff of 450 eV was employed. The Broyden method was employed to relax geometries until the maximum forces on all atoms of 0.05 eV/Å were fulfilled. To obtain simulated $Ru_xIr_yO_2$ system, a large $p(4\times1)$ $IrO_2(110)$ was utilized with different Ru/Ir ratio introduced at the top two atomic layers (see Fig. S1), a k-point of $2\times3\times1$ was employed for the all these $p(4\times1)$ surfaces. During the structural optimization, the bottom two layers of the slab were fixed, and the top two layers of the slab and adsorbates were allowed to be fully relaxed. To estimate and compare the activity trend of the oxygen evolution reaction (OER) on various $Ru_xIr_yO_2$ systems with and without $H_2O*/OH*/O*$ covered on surfaces, the following common mechanism in acidic/neutral environment were considered [4-8]:

$$H_2O + * \rightarrow OH* + H^+ + e \tag{1}$$

$$OH* \rightarrow O* + H^+ + e \tag{2}$$

$$H_2O + OH* \rightarrow OOH* + H^+ + e \tag{3}$$

$$OOH* \rightarrow O_2 + * + H^+ + e \tag{4}$$

where "*" represents the active site for OER, and OH*, O* and OOH* represent the adsorption of OH, O and OOH on active site, respectively. Notably, the computational hydrogen electrode model was used to present the chemical potentials of protons and electrons at any given pH and applied potential (U) [8,9], and thus the Gibbs free energy change ΔG_i of each step above (i = 1, 2, 3 and 4) can be written as:

$$\Delta G_1 = \Delta G_{OH} - eU$$

$$\Delta G_2 = \Delta G_O - \Delta G_{OH} - eU$$

$$\Delta G_3 = \Delta G_{OOH} - \Delta G_O - eU$$

$$\Delta G_4 = 4.92 - \Delta G_{OOH} - eU$$

where ΔG_O, ΔG_{OH} and ΔG_{OOH} are the Gibbs adsorption energies of O, OH and OOH on active centers respectively, which are calculated relative to H_2O and H_2 at $U = 0$ V (vs. standard hydrogen electrode, SHE) and pH = 0. Due to the difficulty of

GGA-DFT in calculating the bond energy of O_2, the experimental formation energy of two H_2O molecules (4.92 eV) was used to calculate the energy of O_2. U is the potential measured against SHE and was set to 0 V. Thus, the theoretical overpotential (η) can be obtained from the Gibbs free energy change ΔG_i (i = 1, 2, 3 and 4) of each step above:

$$\eta = \max(\Delta G_1, \Delta G_2, \Delta G_3, \Delta G_4)/e - 1.23 \text{ (V)}$$

which is independent of pH explicitly and therefore can be used to assess the OER activity trends of $Ru_xIr_yO_2$ catalysts in neutral environment. The obtained theoretical overpotentials of Ru and Ir sites in $Ru_xIr_yO_2(110)$ are summarized in Table S1.

The adsorption energies of adsorbate X (X represents O, OH and OOH) were calculated with the equation: $\Delta G(X) = G_{x/surf} - G_{surf} - G_x$, where G_x, G_{surf} and $G_{x/surf}$ are the total Gibbs free energies of adsorbate X, the clean surface, and the optimized surface with X adsorbed, respectively. The more negative $\Delta G(X)$ means the stronger adsorption of adsorbates on the surface. It is worth noting that, the terms of G_x, G_{surf} and $G_{x/surf}$ were calculated including the zero-point energy (ΔE_{ZPE}) and the entropy effect term ($T\Delta S$), in which the vibrational frequencies of all optimized structures were calculated by DFT calculations [10,11]; with respect to H_2, O_2 in gas phase and H_2O in liquid phase, the related zero-point energy (ΔE_{ZPE}) and entropy effect term ($T\Delta S$) have been reported by other works [6].

1.2 Materials

Ruthenium chloride hydrate ($RuCl_3 \cdot xH_2O$), sodium hexachloroiridate hydrate ($Na_3IrCl_6 \cdot xH_2O$), propylene oxide ($\geq$99%), Nafion® (5 wt% in a mixture of lower aliphatic alcohols and water), ruthenium oxide (RuO_2) and iridium oxide (IrO_2) were purchased from Sigma-Aldrich. Potassium dihydrogen phosphate (KH_2PO_4), dibasic sodium phosphate heptahydrate ($Na_2HPO_4 \cdot 7H_2O$), ammonium sulfate (($NH_4)_2SO_4$), magnesium sulfate ($MgSO_4$), calcium sulfate dihydrate ($CaSO_4 \cdot 2H_2O$), nickel sulfate hexahydrate ($NiSO_4 \cdot 6H_2O$), ferric citrate pentahydrate ($FeC_6H_5O_7 \cdot 5H_2O$), sodium bicarbonate ($NaHCO_3$), N, N-dimethylformamide (DMF), ethanol, isopropanol and acetone were purchased from Sinopharm Chemical Reagent Co., Ltd. Carbon fiber felt was purchased from Nantong Beierge Activated Carbon Fiber Co., Ltd. Carbon black

(20 nm in diameter) was purchased from Suzhou Tanfeng Co., Ltd. Carbon paper was purchased from Toray. All chemicals were used without any further purification.

1.3 Synthesis of catalysts

The Ru-Ir binary oxide (denoted as $Ru_xIr_yO_2$ in the following discussion) catalysts were synthesized *via* a sol-gel method [12]. A typical synthesis procedure is summarized as follows: metal salt precursors (0.4 mmol $RuCl_3 \cdot xH_2O$ and 0.1 mmol $Na_3IrCl_6 \cdot xH_2O$) were first dissolved in 4 mL DMF. The solution was sealed and cooled in a refrigerator for 2 h in order to prevent uncontrolled hydrolysis. Then, 0.5 mL propylene oxide was slowly dropwise added under stirring. The mixed solution was then sealed and aged for 1 day and black precipitates would appear. Afterwards, the solution and precipitates were transferred into a vial and immersed in acetone for 3 days, before the precipitates were collected by centrifugation and washing with acetone for 5 times to thoroughly remove DMF and propylene oxide. The precipitates were dried in vacuum and then grinded carefully. Finally, the as-obtained black powder was placed into a tube furnace and annealed at 400 ^{o}C in air for 2 h to obtain $Ru_xIr_yO_2$ catalyst. Accordingly, $Ru_xIr_yO_2$ catalyst with various feed ratios of Ru/Ir salt precursors (1/8, 1/4, 1/1, 8/1) are also synthesized *via* similar procedure.

1.4 Characterizations of catalysts

The X-ray diffraction (XRD) patterns were collected from a MiniFlex600 X-ray diffractometer with Cu K$_\alpha$ radiation (λ = 0.1542 nm) under a voltage of 40 kV and a current of 40 mA. Transmission electron microscopy (TEM) and corresponding energy dispersive X-ray spectroscopy (EDS) elemental mapping images were obtained using a JEOL JEM-2100 TEM equipped with an Oxford energy disperse spectrometer. The $Ru_xIr_yO_2$ catalyst were subjected to neutral OER reaction before TEM observation. The TEM samples were prepared by dropping catalyst powder dispersed in ethanol onto carbon-coated copper grids, and were dried in vacuum for 6 h. The molar ratio of metal elements for $Ru_xIr_yO_2$ catalyst was quantified by inductively coupled plasma-mass spectrometry (ICP-MS, iCAP7400, Thermo Fisher). X-ray photoelectron spectroscopy (XPS) were obtained using a VG ESCALAB 220I-XL device. All XPS spectra were corrected using C1s line at 284.8 eV. Low

energy ion scattering measurements were performed using a Qtac-100 (ION-TOF) device.

1.5 Electrochemical measurements

Electrochemical measurements were performed in a three-electrode configuration by an electrochemical workstation (MULTI Autolab M204), using Ag/AgCl (with 3.5 M KCl as the filling solution) as the reference electrode and platinum foil as the counter electrode. To prepare the catalyst film on glassy carbon electrodes (GCEs, 3 mm in diameter), 10 mg catalyst and 2 mg carbon black were dispersed in 1.25 mL mixture of water and ethanol (4:1, *v/v*), and then 80 µL of 5 wt. % Nafion® solution was added. The suspension was sonicated for 40 min to obtain a homogeneous ink. Afterwards, 4 µL of the catalyst ink was carefully deposited onto the GCE, with catalyst loading of 0.43 mg/cm². To deposit the catalysts on gold foam and carbon paper electrodes, 20 mg of catalyst powders were dispersed in a 4 mL mixture of water and ethanol (1:1, *v/v*), followed by the addition of 100 µL of 5 wt. % Nafion® solution. The suspension was sonicated for 40 min to prepare a homogeneous ink. Gold foam with a fixed area of 0.5×0.5 cm² coated with water resistant silicone glue was drop-casted with 400 µL of the catalyst ink. Carbon paper with a fixed area of 0.5×0.5 cm² coated with water resistant silicone glue was drop-casted with 200 µL of the catalyst ink.

To evaluate the OER catalytic activity, the working electrode was first scanned from 0.6 to 0.9 V (*vs.* Ag/AgCl) at a scan rate of 50 mV/s for 20 cycles to achieve stable cyclic voltammetry (CV) scans in CO_2-saturated 0.5 M $KHCO_3$ aqueous electrolyte. Then linear sweep voltammetry (LSV) with a scan rate of 1 mV/s was measured. Unless otherwise stated, all CV and LSV measurements were conducted at room temperature (23±2 °C). All the potentials were referred to reversible hydrogen electrode (RHE) by following calculations:

$$E_{RHE} = E_{Ag/AgCl} + 0.2046 + 0.059 \times pH$$

The OER stability of catalysts was evaluated by galvanostatic measurement performed at a constant current density of 10 mA/cm²$_{geo}$ (the currents are normalized to projected geometric areas). During the galvanostatic measurement, a continuous flow of CO_2 gas (99.99% purity) into the aqueous electrolyte was maintained. The electrochemical cell was placed in a 25±2 °C thermostatic waterbath during the test.

1.6 Electrochemical active surface area (ECSA) calculations

The ECSA of catalysts were calculated based on their electrical double layer capacitor (C_{dl}), which were obtained from CV plots in a narrow non-Faradaic potential window from 0.175 to 0.275 V (*vs.* Ag/AgCl). The anodic currents at 0.225 V (*vs.* Ag/AgCl) were plotted as a function of scan rate. Then linear fitting was adopted to these points, and the slope of plots gave the value of C_{dl}. The ECSA value of catalyst was deduced from C_{dl} by dividing a factor of 0.035 mF/cm^2, according to the previous report [13]. The specific activity of catalyst was revealed by normalizing the current to the ECSA value to exclude the effect of surface area on catalytic activity. The ECSA values and specific activities of catalysts are listed at Table S2.

1.7 Turnover frequencies (TOFs) calculations

TOF is defined as the frequency of reaction per active site, which is used to compare the intrinsic activity of each catalyst [14]. The TOFs of catalysts on GCEs in this study were calculated by the following equation:

$$TOF = \frac{j \times A}{4 \times F \times n}$$

where j is the current density obtained at 1.63 V (*vs.* RHE), A is the geometric area, F is the Faraday constant, and n is the mole number of active sites on electrode that is calculated *via* the total loading mass from the following equation:

$$n = \frac{m_{loading}}{Mw} \times r$$

where $m_{loading}$ is the loading mass of catalyst on GCE, Mw is the molecular weight of catalyst and r is the molar ratio of active atoms in the catalyst. In this work, the Ir/Ru atomic ratio of $Ru_xIr_yO_2$ catalyst is 0.5 according to the results from ICP-MS analysis. The TOF values of catalysts are listed at Table S2.

1.8 Bioelectrochemical reactor for synthesis of poly(3-hydroxybutyrate) (PHB)

The water splitting and CO_2 fixation by microorganisms took place in a single sealed chamber. The reactor is a 150 mL glass bottle with a 4-ports connection system on the cap and 2 ports on the bottle body. The reactor was placed in a room at a constant temperature of 30 ℃. The two ports of the cap were used to insert electrodes, while the third one served as gas inlet controlled by a flowmeter and the last one was

connected to the ambient atmosphere through a gas filter. Two ports on the bottle body are used for injection and sampling.

For a typical experiment, 90 mL minimal medium solution bubbled with CO_2 was added into the reactor, and water splitting was performed *via* a two-electrode configuration. The composition of minimal medium was $Na_2HPO_4 \cdot 7H_2O$ (3.57 g/L), KH_2PO_4 (1.5 g/L), $(NH_4)_2SO_4$ (1.0 g/L), $MgSO_4$ (39.07 mg/L), $CaSO_4 \cdot 2H_2O$ (1 mg/L), $NiSO_4 \cdot 6H_2O$ (0.524 mg/L), $FeC_6H_5O_7 \cdot 5H_2O$ (0.547 mg/L) and $NaHCO_3$ (200 mg/L). The $Ru_xIr_yO_2$ catalysts deposited onto carbon fiber felt are used as anode and $CoW(OH)_x$ catalysts deposited onto carbon fiber felt are used as cathode [15]. After inoculation with *R. eutropha* strains [16], the reactor was sealed and bubbled with CO_2 gas under stirring. The electrolyte was sampled daily to monitor and quantify the bacterial growth and biomass product accumulation.

The bacterial growth was measured by determining the optical density at 600 nm (OD_{600}) of the electrolyte sample taken from the reactor. A 650 nm laser pointer was directed at a photodiode across the cuvette containing bacteria and electrolyte. The standard curve between the measured light intensity and OD_{600} was established, after measuring the transmitted light from *R. eutropha* cultures of known OD_{600} values. For quantification of the PHB product, the electrolyte sample taken from the reactor was first centrifuged at 12000 rpm for 1 min. The cell pellet and PHB standard substance (Sigma 363502) were digested into 3-hydroxybutyrate with concentrated H_2SO_4 at 90 ℃ for 1 h. The digestion dilution was sequentially diluted with deionized water by 50 times and filtered with 0.22 μm filter. The pretreated samples were determined by a high-performance liquid chromatography system (Waters, e2695) equipped with a 2998 PDA detector (210 nm). An Aminex HPX-87H column was used at 35 ℃ with 4 mM H_2SO_4 as the mobile phase at a flow rate of 0.6 mL/min for 30 min. The elution time was ~28 min for the PHB product [16].

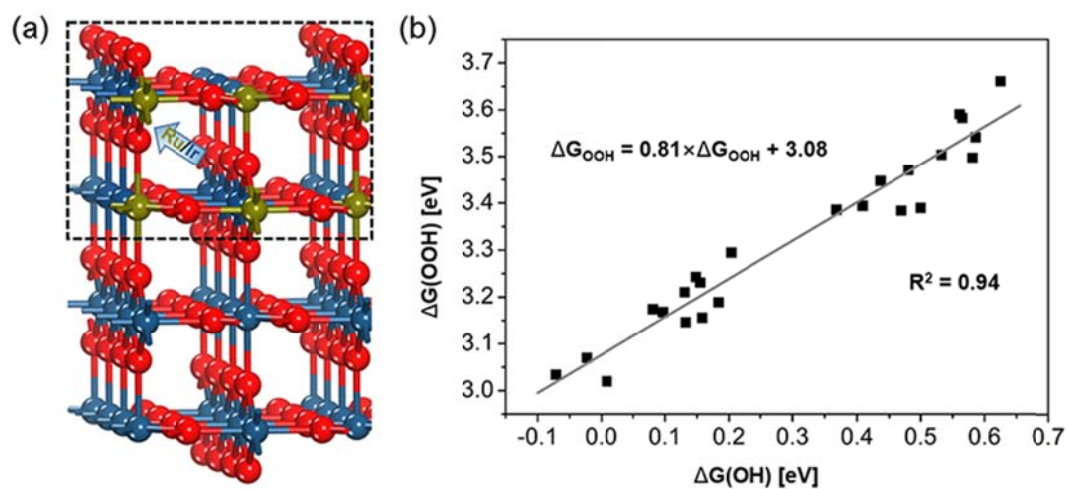## 2   Supplementary Figures

Figure S1. (a) The uniform solid solution model of $Ru_xIr_yO_2(110)$, with the Ru/Ir ratio increased along the direction of arrow, where Ru/Ir ratio of 25%, 50% and 75% are considered. The blue and green balls represent Ir and Ru atoms, respectively. **(b)** The relationship of the adsorption energies of OOH* ($\Delta G(OOH)$) as a function of the adsorption energy of OH* ($\Delta G(OH)$) on $Ru_xIr_xO_2(110)$ model.
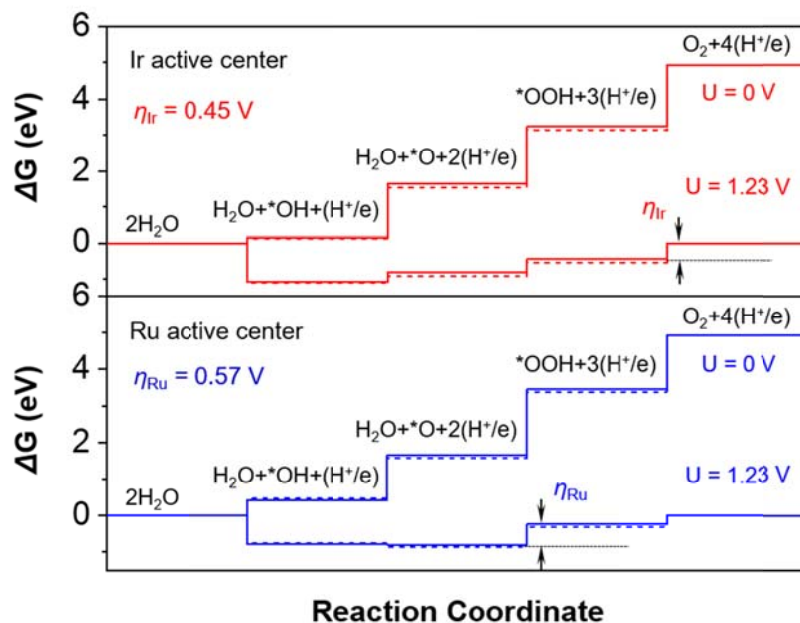
Figure S2. The free-energy profiles of OER catalyzed by the Ir or Ru active site on clean $Ru_{0.5}Ir_{0.5}O_2(110)$ model (dotted line) and O*-covered $Ru_{0.5}Ir_{0.5}O_2(110)$ model (solid line).

As shown in Figure S2, the adsorption energies of OOH* intermediates on Ir active centers in rate-determining step are decreased on O*-covered $Ru_xIr_yO_2(110)$ model, compared with that on clean $Ru_xIr_yO_2(110)$ model, indicating that O* species adsorbed on Ru sites (Ru=O species) can enhance the OER activities of adjacent Ir active sites.
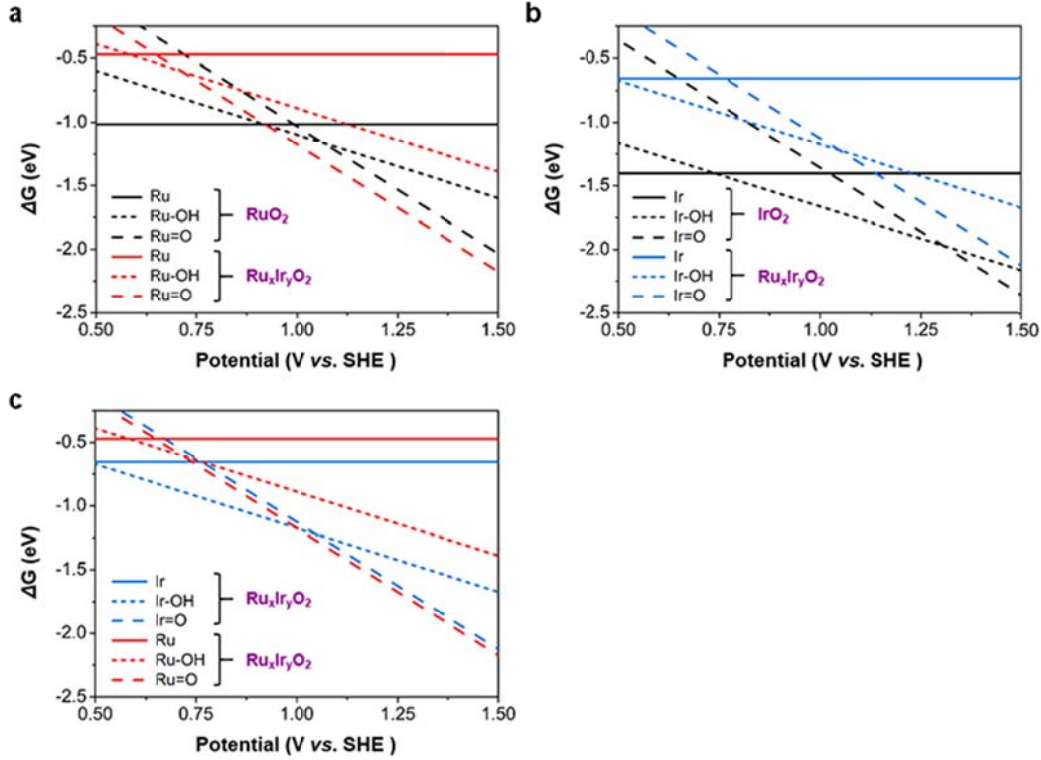
Figure S3. (a, b, c) The surface phase diagrams of $Ru_{0.5}Ir_{0.5}O_2(110)$, $RuO_2(110)$ and $IrO_2(110)$ models under the actual neutral OER conditions (pH = 7), respectively.

Under the actual neutral OER conditions, the activation of water can form various surface intermediates on the active sites, leading to different surface phases. Here, three different states were considered: water molecule covered surface (H_2O^*), hydroxyl covered surface (HO^*), and oxygen covered surface (O^*). The reactions forming the different states on surface can be written as:

$$H_2O + * \rightarrow H_2O + *$$

$$H_2O + * \rightarrow HO^* + H^+ + e$$

$$H_2O + * \rightarrow O^* + 2H^+ + 2e$$
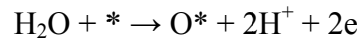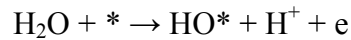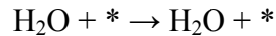
where * represents the active site (Ir or Ru). The Gibbs free energy change of the above three steps was calculated as $\Delta G(U) = \Delta G(0) - neU + n\Delta G_{H+}$ (pH), where $\Delta G(0)$ is the free energy change of reaction at $U = 0$ V and pH = 0, and $\Delta G(U)$ is the free energy change of reaction at the applied potential (U) and pH = 7. The free energy change of H^+ relative to the above specified electrode at non-zero pH is represented by the Nernst equation as ΔG_{H+} (pH)$= -k_B \times T \times \ln(10) \times pH$. Then, the surface phase diagram (pH = 7) on Ir or Ru active sites on RuO_2, IrO_2 and $Ru_xIr_yO_2$ as a function of the applied U can be obtained (Fig. S3).

The surface phase diagrams (Fig. S3a and S3b) show that the formation of Ru=O (Ir=O) on $Ru_xIr_yO_2$ surface, corresponding to the adsorbed O* species on Ru (Ir), is promoted (suppressed) compared to that on RuO_2 (IrO_2). Notably, the formation of Ru=O is more thermodynamically favorable than that of Ir=O on $Ru_xIr_yO_2$ with the applied potential above 1.0 V (Fig. S3c). Thus, the existence of Ru=O species adjacent to the Ir active center in $Ru_xIr_yO_2$ system under the actual neutral OER conditions (pH = 7) can be anticipated. At the same time, owing to the higher OER activities of Ir active sites than those of Ru active sites, the Ir=O species at steady state would be easier to converse compared to Ru=O species. Thus, the amount of Ru=O species will be larger than that of Ir=O species on $Ru_xIr_yO_2$ surface.
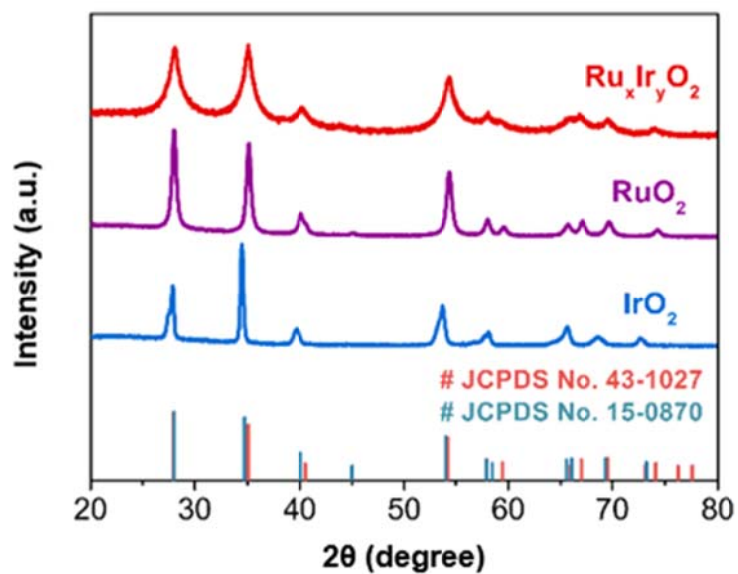
Figure S4. XRD patterns of $Ru_xIr_yO_2$ catalyst and controls (benchmark RuO_2 and IrO_2 catalysts). The characteristic peaks of the synthesized $Ru_xIr_yO_2$ catalyst can be indexed to RuO_2 (JCPDS card No. 43-1027) and IrO_2 (JCPDS card No.15-0870) in rutile phase.

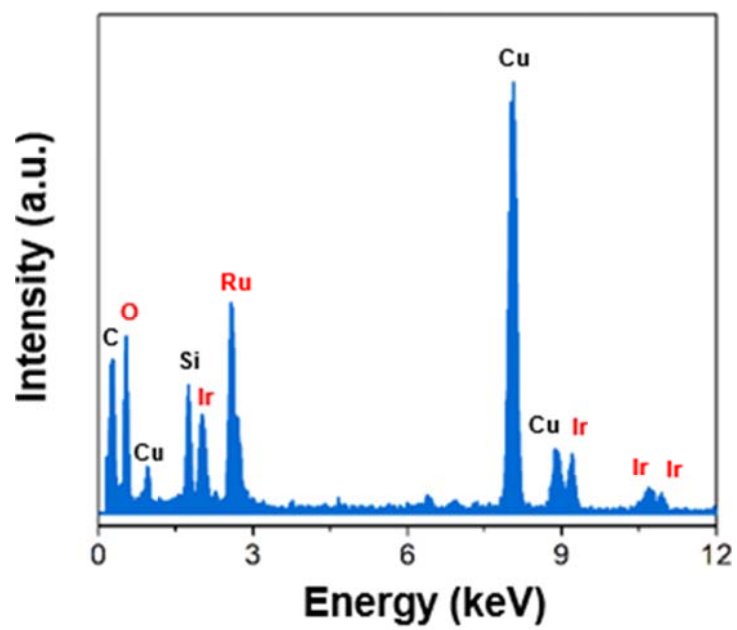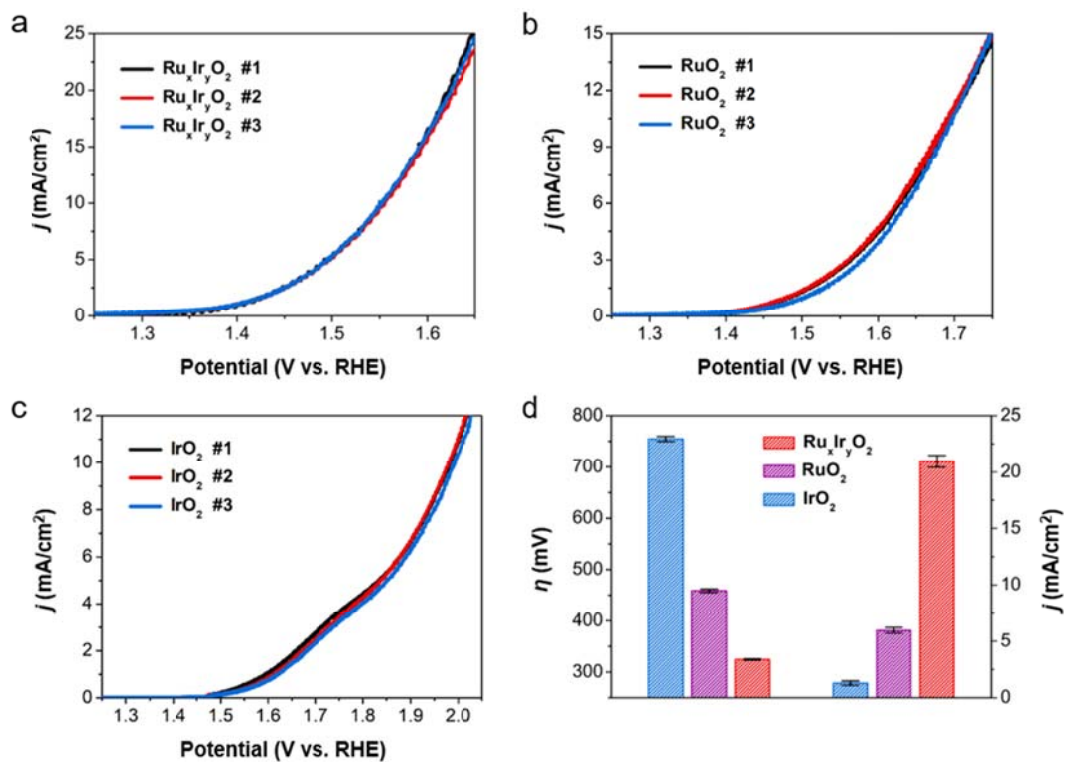**Figure S5.** EDS spectrum of $Ru_xIr_yO_2$ catalyst.

Figure S6. (a-c) Three independent LSV tests for $Ru_xIr_yO_2$ catalyst and controls on GCEs measured at a scan rate of 1 mV/s in CO_2-saturated 0.5 M $KHCO_3$ aqueous electrolyte. **(d)** Summary of overpotential (η) at 10 mA/cm$^2_{geo}$ and current density (j) at 1.63 V (*vs.* RHE) for catalyst on GCE.

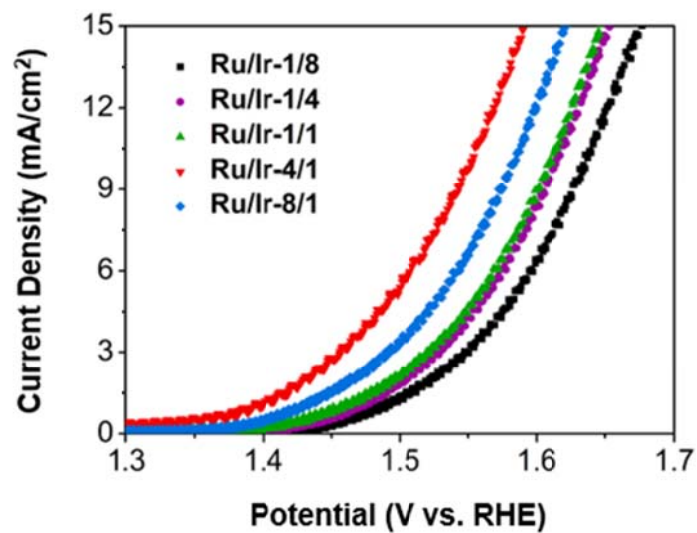**Figure S7.** LSV curves of $Ru_xIr_yO_2$ catalysts with different Ru/Ir feed ratios on GCEs at a scan rate of 1 mV/s in CO_2-saturated 0.5 M $KHCO_3$ aqueous electrolyte.
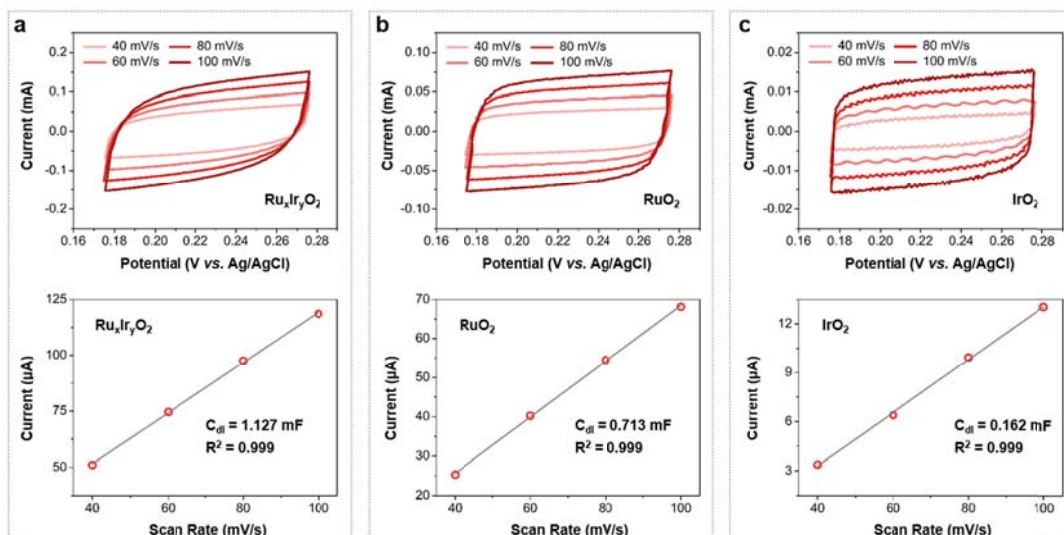
Figure S8. The ECSA measurements of Ru$_x$Ir$_y$O$_2$ catalyst and controls on GCEs. CV scans were carried out at non-Faradic windows from 0.175 to 0.275 V (*vs.* Ag/AgCl). The current as a function of scan rate gives the C$_{dl}$ for each catalyst.
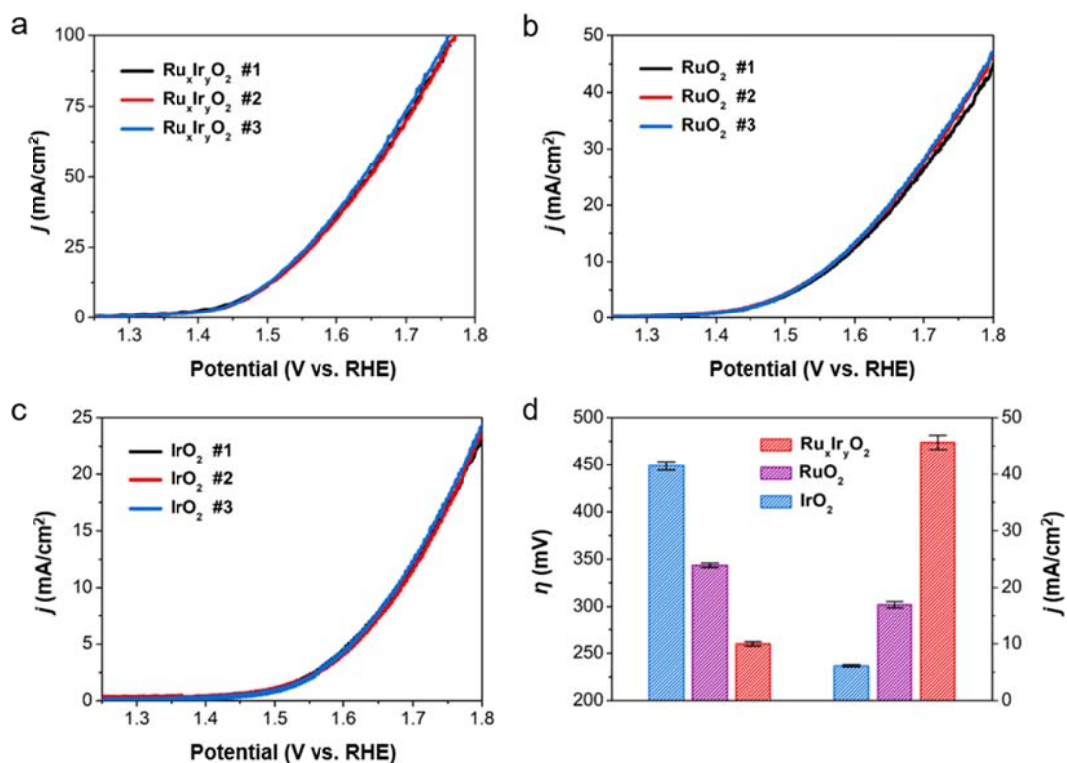
Figure S9. **(a-c)** Three independent LSV tests for $Ru_xIr_yO_2$ catalyst and controls on gold foam electrodes measured at a scan rate of 1 mV/s in CO_2-saturated 0.5 M $KHCO_3$ aqueous electrolyte. **(d)** Summary of overpotential (η) at 10 mA/cm$^2_{geo}$ and current density (j) at 1.63 V (*vs.* RHE) for catalyst on gold foam electrode.
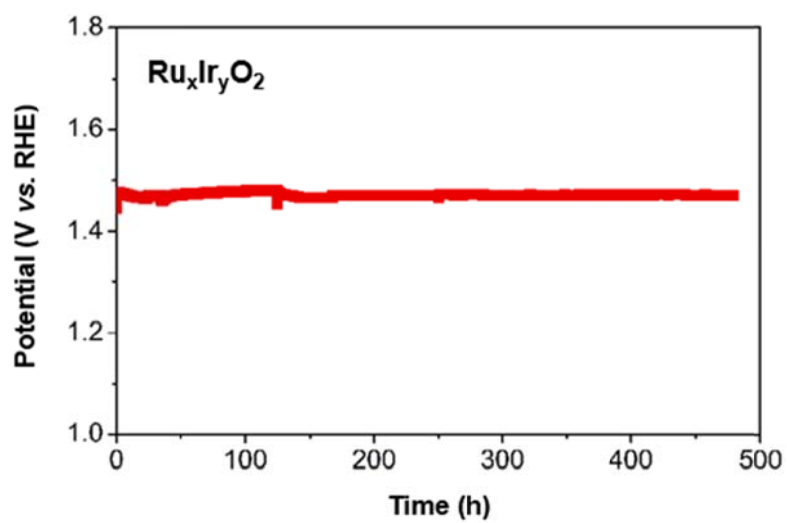
Figure S10. Chronopotentiometric curves obtained with $Ru_xIr_yO_2$ catalyst on gold foam electrode at a constant current density of 10 mA/cm^2_{geo}.
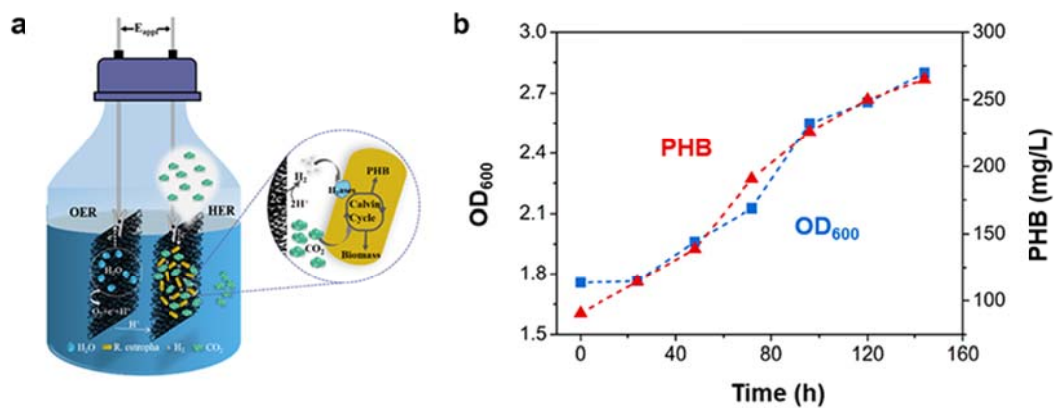
Figure S11. (a) Schematic of microbial electrosynthesis system to reduce CO_2 for the biosynthesis of PHB product. In this system, electrochemical water splitting produces H_2 as electron carrier, which is oxidized by hydrogenases and fuels *R. eutropha* strains to assimilate CO_2 through Calvin cycle to produce PHB. **(b)** The measured results of OD_{600} (indicator of bacterial growth) and PHB product titers in the reactor accumulated during the process of biosynthesis.

Figure S12. (a-c) Three independent LSV tests obtained with $Ru_xIr_yO_2$ catalyst ("as is") and after heating at 150 ℃ in vacuum ("as is + 150") on gold foam electrodes measured at a scan rate of 1 mV/s in CO_2-saturated 0.5 M $KHCO_3$ aqueous electrolyte. **(d)** Summary of overpotentials (η) at 10 mA/cm$^2_{geo}$ for the $Ru_xIr_yO_2$ catalyst on gold foam electrodes before and after heating at 150 ℃ in vacuum.
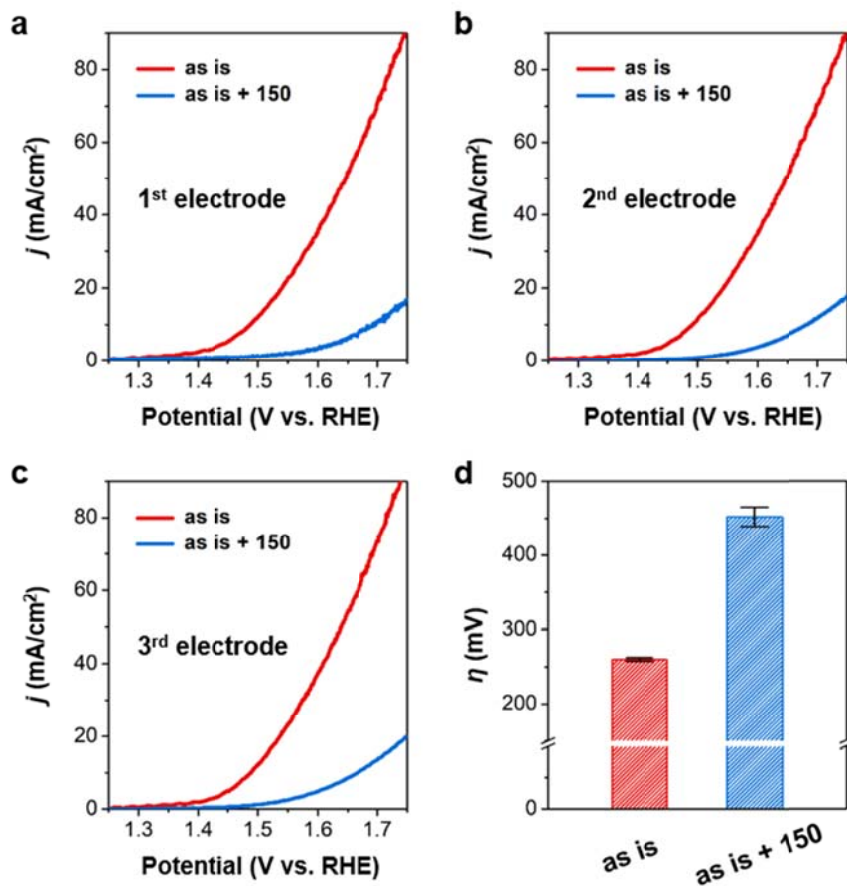
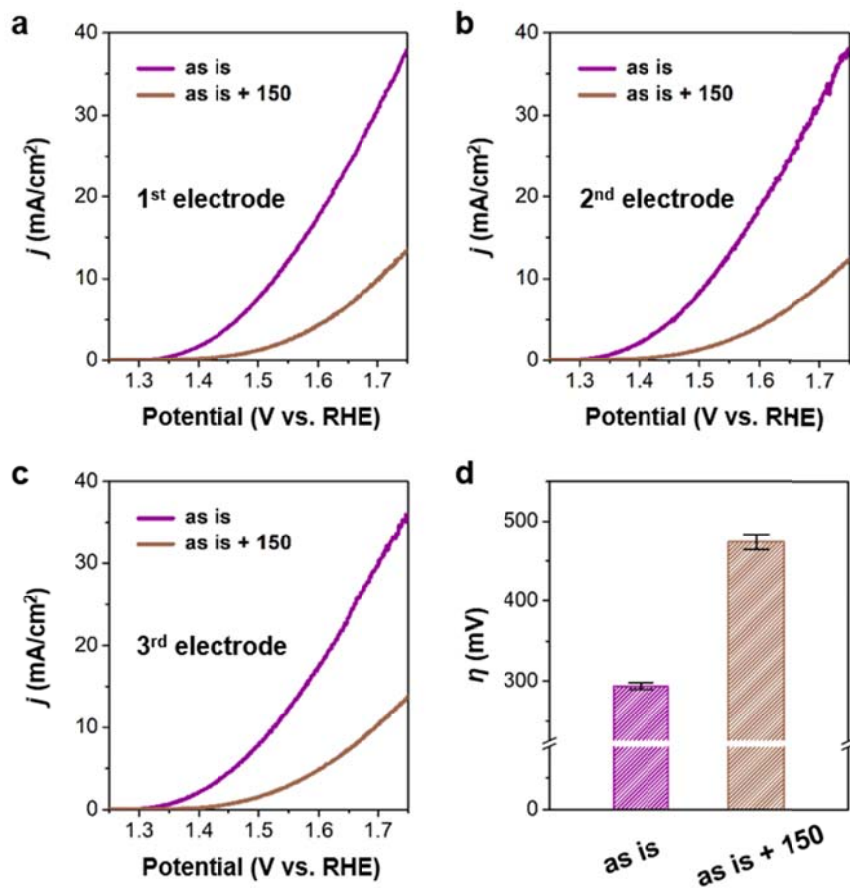**Figure S13. (a-c)** Three independent LSV tests obtained with $Ru_xIr_yO_2$ catalyst ("as is") and after heating at 150 ℃ in vacuum ("as is + 150") on carbon paper electrodes at a scan rate of 5 mV/s in CO_2-saturated 0.5 M $KHCO_3$ aqueous electrolyte. **(d)** Summary of overpotentials (η) at 10 mA/cm^2_{geo} for $Ru_xIr_yO_2$ catalyst on carbon paper electrodes before and after heating at 150 ℃ in vacuum.
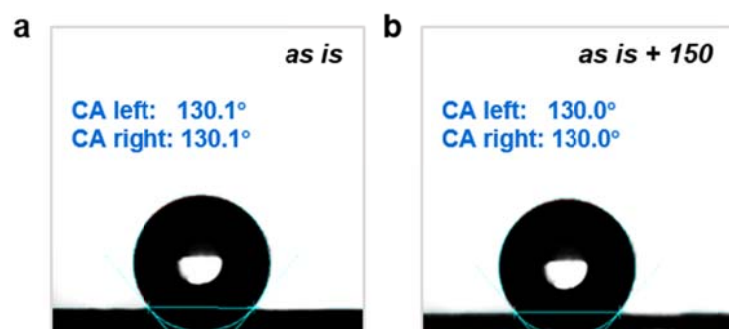
Figure S14. (a, b) Static water contact-angle measurements of $Ru_xIr_yO_2$ ("as is") and after heating at 150 ℃ in vacuum ("as is + 150"), respectively. The contact angles remained almost unchanged, which indicated their similar surface hydrophilicity.
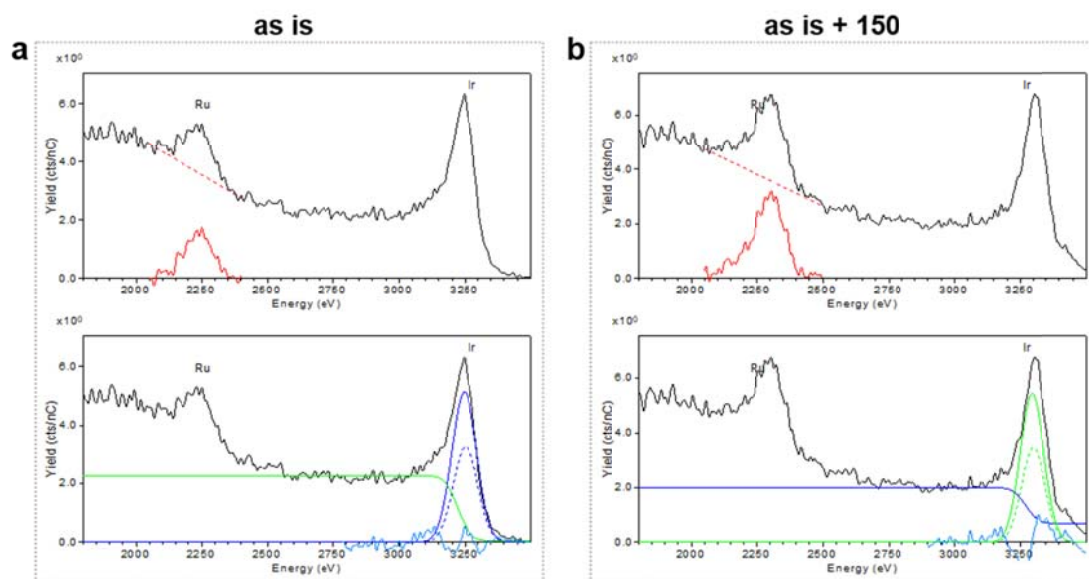
Figure S15. (**a, b**) LEIS spectra and corresponding peak fitting results of Ir/Ru atomic ratios for $Ru_xIr_yO_2$ catalyst ("as is") and after *in-situ* heating at 150 ℃ in vacuum ("as is + 150"), respectively.

As shown in Figure S15, the Ir/Ru atomic ratio at topmost atomic layers of $Ru_xIr_yO_2$ catalyst is calculated according to the fitting peak areas of Ru and Ir peaks observed in the LEIS spectra.
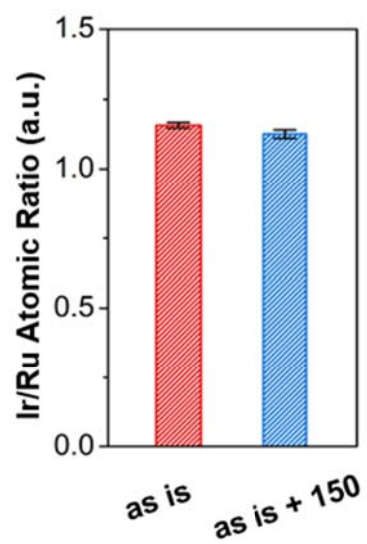
Figure S16. The bulk Ir/Ru atomic ratios of $Ru_xIr_yO_2$ catalyst ("as is") and after heating at 150 ℃ in vacuum ("as is + 150") obtained from XPS measurements.
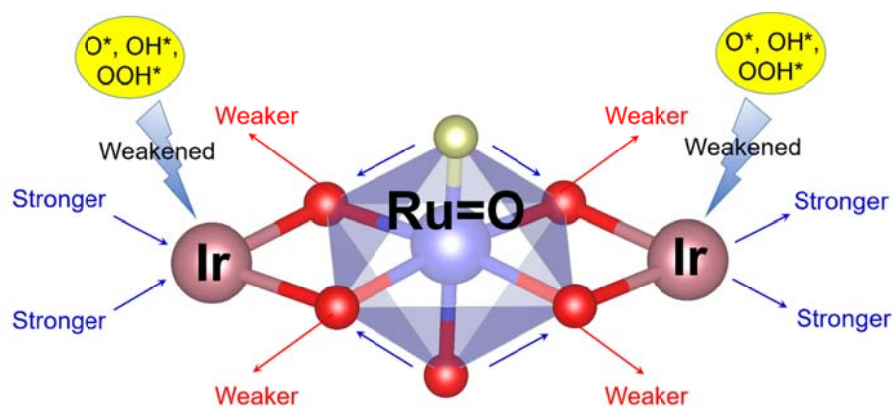
Figure S17. The bond order conservation principle diagram of adjacent Ru=O species decreasing the adsorption energies of OER intermediates (e.g. O*, OH* and OOH*) on the Ir active center, thus yielding enhanced activity of Ir active center, when taking into account the surface dual-metal-sites as a whole.

3 Supplementary Tables

Table S1. Theoretical overpotentials of Ru and Ir sites on $Ru_xIr_yO_2(110)$ with different Ru/Ir atomic ratios under different surface environments.

	Ru	Ru (Ir-H$_2$O)	Ru (Ir-OH)	Ru (Ir=O)	Ir	Ir (Ru-H$_2$O)	Ir (Ru-OH)	Ir(Ru=O)
IrO$_2$	\	\	\	\	0.67	\	\	\
Ru$_{0.25}$Ir$_{0.75}$O$_2$	0.57	0.68	0.58	0.57	0.54	0.59	0.52	0.45
Ru$_{0.5}$Ir$_{0.5}$O$_2$	0.54	0.64	0.56	0.57	0.54	0.58	0.52	0.46
Ru$_{0.75}$Ir$_{0.25}$O$_2$	0.55	0.64	0.54	0.56	0.50	0.57	0.48	0.39
RuO$_2$	0.62	\	\	\	\	\	\	\

Table S2. Summary of electrochemical performance of each catalyst on GCE.

Sample	η^1 (mV)	C_{dl} (mF)	ECSA area (cm^2)	Mass activity (A/g)	Specific activity^2 (mA/cm^2)	TOF^3 (s^{-1})	TOF^4 (s^{-1})
Ru$_x$Ir$_y$O$_2$	324±1	1.127	32.20	49.25	0.046	0.159	0.326
RuO$_2$	459±3	0.713	20.37	14.03	0.021	0.048	0.048
IrO$_2$	755±5	0.162	4.63	3.03	0.020	0.009	0.009

[1] Overpotential at 10 mA/cm$^2_{geo}$.

[2] Calculated according to ECSA area. η=400 mV.

[3] Calculated according to mass loading of all metal atoms. η=400 mV.

[4] Calculated according to mass loading of all active sites. η=400 mV.

Table S3. Summary of recently reported OER electrocatalysts in neutral media.

Sample	pH	On GCE η at 10 mA/cm^2 (mV)	On Foam η at 10 mA/cm^2 (mV)	Reference
Our catalyst	**7.2**	**324±1**	**260±2**	**This work**
Co_4Mo	7.2	456		[17]
NiFeCoP	7.2	560	330	[18]
IrO_2	7.1	520[a]		[19]
NiFeMg	7.2	514	310	[20]
$(Fe_xNi_{1-x})_2P$	7.0		396	[21]
CoO/Co_4N	7.0		398	[22]
Co_2P	7.0	592		[23]
Co-Pi	7.0		450[b]	[24]
CoO	7.0	851		[25]
Ni	7.0		600	[26]
IrO_x/CN_xNTs	7.0		472	[27]
IrO_2	7.2		460[c]	[28]

a. FTO glass

b. Ti mesh

c. Ti plate

Table S4. Summary of other reported biosynthesis systems from CO_2 fixation.

Microorganism	Voltage of full cell (V)	Current density (mA/cm^2)	Product	Selectivity (%)	Reference
R. eutropha H16	**1.8**	**4.5**	**PHB**	**100**	**This work**
R. eutropha H16	2.0	~ 4.5	PHB	100	[29]
R. eutropha H16	2.7	3.75	biomass	-	[30]
R. eutropha Re2133-pEG12	3.0	9.5	isopropanol	100	[30]
S. ovata	3.0	~ 7.1	acetate	100	[31]
R. eutropha LH74D	~ 4	16.7	isobutanol + 3-methy-1-butanol	94.6	[32]
R. eutropha H16	~ 5	-	biomass	-	[33]

References for the Supplementary Information:

1. Perdew JP, Ruzsinszky A, Csonka GI, *et al*. Restoring the density-gradient expansion for exchange in solids and surfaces. Phys Rev Lett, 2008, 100: 136406

2. Kresse G, Furthmuller J. Efficient iterative schemes for *ab* initio total-energy calculations using a plane-wave basis set. Phys Rev B, 1996, 54: 11169-11186

3. Kresse G, Joubert D. From ultrasoft pseudopotentials to the projector augmented-wave method. Phys Rev B, 1999, 59: 1758-1775

4. Rossmeisl J, Qu ZW, Zhu H, *et al*. Electrolysis of water on oxide surfaces. J Electroanal Chem, 2007, 607: 83-89

5. Valdes A, Qu ZW, Kroes GJ, *et al*. Oxidation and photo-oxidation of water on TiO_2 surface. J Phys Chem C, 2008, 112: 9872-9879

6. Liao P, Keith JA, Carter EA. Water oxidation on pure and doped hematite (0001) surfaces: Prediction of Co and Ni as effective dopants for electrocatalysis. J Am Chem Soc, 2012, 134: 13296-13309

7. Bajdich M, Garcia-Mota M, Vojvodic A, *et al*. Theoretical investigation of the activity of cobalt oxides for the electrochemical oxidation of water. J Am Chem Soc, 2013, 135: 13521-13530

8. Friebel D, Louie MW, Bajdich M, *et al*. Identification of highly active Fe sites in (Ni,Fe)OOH for electrocatalytic water splitting. J Am Chem Soc, 2015, 137: 1305-1313

9. Norskov JK, Rossmeisl J, Logadottir A, *et al*. Origin of the overpotential for oxygen reduction at a fuel-cell cathode. J Phys Chem B, 2004, 108: 17886-17892

10. Xu J, Li X, Liu W, *et al*. Carbon dioxide electroreduction into syngas boosted by a partially delocalized charge in molybdenum sulfide selenide alloy monolayers. Angew Chem Int Ed, 2017, 56: 9121-9125

11. Yuan H, Sun N, Chen J, *et al*. Insight into the NH_3-assisted selective catalytic reduction of NO on *beta*-MnO_2(110): Reaction mechanism, activity descriptor, and evolution from a pristine state to a steady state. ACS Catal, 2018, 8: 9269-9279

12. Zhang B, Zheng XL, Voznyy O, *et al*. Homogeneously dispersed multimetal oxygen-evolving catalysts. Science, 2016, 352: 333-337

13. Kim YT, Lopes PP, Park SA, *et al*. Balancing activity, stability and conductivity of nanoporous core-shell iridium/iridium oxide oxygen evolution catalysts. Nat

Commun, 2017, 8: 1449

14. McCrory CCL, Jung S, Peters JC, *et al*. Benchmarking heterogeneous electrocatalysts for the oxygen evolution reaction. J Am Chem Soc, 2013, 135: 16977-16987

15. Zhang L, Liu PF, Li YH, *et al*. Accelerating neutral hydrogen evolution with tungsten modulated amorphous metal hydroxides. ACS Catal, 2018, 8: 5200-5205

16. Chen X, Cao Y, Li F, *et al*. Enzyme-Assisted Microbial Electrosynthesis of Poly(3-hydroxybutyrate) *via* CO_2 Bioreduction by Engineered *Ralstonia eutropha*. ACS Catal, 2018, 8: 4429-4437

17. Xu YT, Ye ZM, Ye JW, *et al*. Non-3d metal modulation of a cobalt imidazolate framework for excellent electrocatalytic oxygen evolution in neutral media. Angew Chem Int Ed, 2019, 58: 139-143

18. Zheng XL, Zhang B, De Luna P, *et al*. Theory-driven design of high-valence metal sites for water oxidation confirmed using in situ soft X-ray absorption. Nat Chem, 2018, 10: 149-154

19. Gurudayal, Bullock J, Sranko DF, *et al*. Efficient solar-driven electrochemical CO_2 reduction to hydrocarbons and oxygenates. Energy Environ Sci, 2017, 10: 2222-2230

20. Wang N, Cao Z, Zheng X, *et al*. Hydration-effect-promoting Ni-Fe oxyhydroxide catalysts for neutral water oxidation. Adv Mater, 2020, 32: 1906806

21. Zhang BW, Lui YH, Ni HW, *et al*. Bimetallic $(Fe_xNi_{1-x})_2P$ nanoarrays as exceptionally efficient electrocatalysts for oxygen evolution in alkaline and neutral media. Nano Energy, 2017, 38: 553-560

22. Li RQ, Hu PF, Miao M, *et al*. CoO-modified Co_4N as a heterostructured electrocatalyst for highly efficient overall water splitting in neutral media. J Mater Chem A, 2018, 6: 24767-24772

23. Xu K, Cheng H, Liu L, *et al*. Promoting active species generation by electrochemical activation in alkaline media for efficient electrocatalytic oxygen evolution in neutral media. Nano Lett, 2017, 17: 578-583

24. Xie LS, Zhang R, Cui L, *et al*. High-performance electrolytic oxygen evolution in neutral media catalyzed by a cobalt phosphate nanoarray. Angew Chem Int Ed,

2017, 56: 1064-1068

25. Tung CW, Hsu YY, Shen YP, *et al*. Reversible adapting layer produces robust single-crystal electrocatalyst for oxygen evolution. Nat Commun, 2015, 6: 8106

26. Schaefer H, Chevrier DM, Zhang P, *et al*. Electro-oxidation of Ni42 steel: A highly active bifunctional electrocatalyst. Adv Funct Mater, 2016, 26: 6402-6417

27. Lv W, Liu S, Zhang R, *et al*. IrO_x/CN_xNTs as electrocatalysts for oxygen evolution reaction in a HCO^{3-}/CO_2 system at neutral pH. J Mater Sci, 2018, 53: 4939-4948

28. Schreier M, Curvat L, Giordano F, *et al*. Efficient photosynthesis of carbon monoxide from CO_2 using perovskite photovoltaics. Nat Commun, 2015, 6: 7326

29. Liu C, Colon BC, Ziesack M, *et al*. Water splitting-biosynthetic system with CO_2 reduction efficiencies exceeding photosynthesis. Science, 2016, 352: 1210-1213

30. Torella JP, Gagliardi CJ, Chen JS, *et al*. Efficient solar-to-fuels production from a hybrid microbial-water-splitting catalyst system. Proc Natl Acad Sci U S A, 2015, 112: 2337-2342

31. Giddings CGS, Nevin KP, Woodward T, *et al*. Simplifying microbial electrosynthesis reactor design. Front Microbiol, 2015, 6: 468

32. Li H, Opgenorth PH, Wernick DG, *et al*. Integrated electromicrobial conversion of CO_2 to higher alcohols. Science, 2012, 335: 1596-1596

33. Schlegel HG, Lafferty R. Growth of *Knallgas* bacteria (hydrogenomonas) using direct electrolysis of culture medium. Nature, 1965, 205: 308-309